

Automated spectroscopic retinal oximetry with visible-light optical coherence tomography

SHAOHUA PI,¹ ACNER CAMINO,¹ WILLIAM CEPURNA,¹ XIANG WEI,¹ MIAO ZHANG,² DAVID HUANG,¹ JOHN MORRISON,¹ AND YALI JIA^{1,*}

¹Casey Eye Institute, Oregon Health & Science University, Portland, OR, USA

²Optovue Inc. 2800 Bayview Dr., Fremont, CA 94538, USA

*jiaya@ohsu.edu

Abstract: Accurate, quantitative assessment of retinal blood oxygen saturation (sO_2) may provide a useful early indicator of pathophysiology in several ocular diseases. Here, with visible-light optical coherence tomography (OCT), we demonstrate an automated spectroscopic retinal oximetry algorithm to measure the sO_2 within the retinal arteries (A- sO_2) and veins (V- sO_2) in rats by automatically detecting the vascular posterior boundary on cross-sectional structural OCT. The algorithm was validated *in vitro* with flow phantoms and *in vivo* in rats by comparing the sO_2 results, respectively, to those obtained using a blood gas analyzer and pulse oximetry. We also investigated the response of oxygen extraction (A-V sO_2), including inter-session reproducibility, at different inhaled oxygen concentrations.

© 2018 Optical Society of America under the terms of the OSA Open Access Publishing Agreement

OCIS codes: (110.4500) Optical coherence tomography; (170.2655) Functional monitoring and imaging; (170.4470) Ophthalmology; (100.2980) Image enhancement.

References and links

1. R. A. Linsenmeier and H. F. Zhang, "Retinal oxygen: from animals to humans," *Prog. Retin. Eye Res.* **58**, 115–151 (2017).
2. J. M. Beach, K. J. Schwenzer, S. Srinivas, D. Kim, and J. S. Tiedeman, "Oximetry of retinal vessels by dual-wavelength imaging: calibration and influence of pigmentation," *J. Appl. Physiol.* **86**(2), 748–758 (1999).
3. J. V. Kristjansdottir, S. H. Hardarson, G. H. Halldorsson, R. A. Karlsson, T. S. Eliasdottir, and E. Stefansson, "Retinal Oximetry With a Scanning Laser Ophthalmoscope," *Invest. Ophthalmol. Vis. Sci.* **55**(5), 3120–3126 (2014).
4. H. F. Zhang, K. Maslov, G. Stoica, and L. V. Wang, "Functional photoacoustic microscopy for high-resolution and noninvasive *in vivo* imaging," *Nat. Biotechnol.* **24**(7), 848–851 (2006).
5. S. Jiao, M. Jiang, J. Hu, A. Fawzi, Q. Zhou, K. K. Shung, C. A. Puliafito, and H. F. Zhang, "Photoacoustic ophthalmoscopy for *in vivo* retinal imaging," *Opt. Express* **18**(4), 3967–3972 (2010).
6. D. Huang, E. A. Swanson, C. P. Lin, J. S. Schuman, W. G. Stinson, W. Chang, M. R. Hee, T. Flotte, K. Gregory, C. A. Puliafito, and J. G. Fujimoto, "Optical coherence tomography," *Science* **254**(5035), 1178–1181 (1991).
7. L. M. Sakata, J. Deleon-Ortega, V. Sakata, and C. A. Girkin, "Optical coherence tomography of the retina and optic nerve - a review," *Clin. Experiment. Ophthalmol.* **37**(1), 90–99 (2009).
8. D. J. Faber, E. G. Mik, M. C. Aalders, and T. G. van Leeuwen, "Toward assessment of blood oxygen saturation by spectroscopic optical coherence tomography," *Opt. Lett.* **30**(9), 1015–1017 (2005).
9. J. Yi, Q. Wei, W. Liu, V. Backman, and H. F. Zhang, "Visible-light optical coherence tomography for retinal oximetry," *Opt. Lett.* **38**(11), 1796–1798 (2013).
10. S. Chen, J. Yi, W. Liu, V. Backman, and H. F. Zhang, "Monte Carlo investigation of optical coherence tomography retinal oximetry," *IEEE Trans. Biomed. Eng.* **62**(9), 2308–2315 (2015).
11. S. Chen, X. Shu, J. Yi, A. Fawzi, and H. F. Zhang, "Dual-band optical coherence tomography using a single supercontinuum laser source," *J. Biomed. Opt.* **21**(6), 066013 (2016).
12. T. Lister, P. A. Wright, and P. H. Chappell, "Optical properties of human skin," *J. Biomed. Opt.* **17**(9), 0909011 (2012).
13. S. P. Chong, M. Bernucci, H. Radhakrishnan, and V. J. Srinivasan, "Structural and functional human retinal imaging with a fiber-based visible light OCT ophthalmoscope," *Biomed. Opt. Express* **8**(1), 323–337 (2017).
14. S. Pi, A. Camino, M. Zhang, W. Cepurna, G. Liu, D. Huang, J. Morrison, and Y. Jia, "Angiographic and structural imaging using high axial resolution fiber-based visible-light OCT," *Biomed. Opt. Express* **8**(10), 4595–4608 (2017).

15. S. P. Chong, C. W. Merkle, C. Leahy, H. Radhakrishnan, and V. J. Srinivasan, "Quantitative microvascular hemoglobin mapping using visible light spectroscopic Optical Coherence Tomography," *Biomed. Opt. Express* **6**(4), 1429–1450 (2015).
16. N. Bosschaart, G. J. Edelman, M. C. Aalders, T. G. van Leeuwen, and D. J. Faber, "A literature review and novel theoretical approach on the optical properties of whole blood," *Lasers Med. Sci.* **29**(2), 453–479 (2014).
17. K. F. Palmer and D. Williams, "Optical properties of water in the near infrared," *JOSA* **64**(8), 1107–1110 (1974).
18. J. Yi and V. Backman, "Imaging a full set of optical scattering properties of biological tissue by inverse spectroscopic optical coherence tomography," *Opt. Lett.* **37**(21), 4443–4445 (2012).
19. Y. Jia, O. Tan, J. Tokayer, B. Potsaid, Y. Wang, J. J. Liu, M. F. Kraus, H. Subhash, J. G. Fujimoto, J. Hornegger, and D. Huang, "Split-spectrum amplitude-decorrelation angiography with optical coherence tomography," *Opt. Express* **20**(4), 4710–4725 (2012).
20. S. S. Gao, G. Liu, D. Huang, and Y. Jia, "Optimization of the split-spectrum amplitude-decorrelation angiography algorithm on a spectral optical coherence tomography system," *Opt. Lett.* **40**(10), 2305–2308 (2015).
21. M. Zhang, J. Wang, A. D. Pechauer, T. S. Hwang, S. S. Gao, L. Liu, L. Liu, S. T. Bailey, D. J. Wilson, D. Huang, and Y. Jia, "Advanced image processing for optical coherence tomographic angiography of macular diseases," *Biomed. Opt. Express* **6**(12), 4661–4675 (2015).
22. J. Yi, W. Liu, S. Chen, V. Backman, N. Sheibani, C. M. Sorenson, A. A. Fawzi, R. A. Linsenmeier, and H. F. Zhang, "Visible light optical coherence tomography measures retinal oxygen metabolic response to systemic oxygenation," *Light Sci. Appl.* **4**(9), e334 (2015).

1. Introduction

Altered oxygen supply is thought to be a critical factor underlying many retinal disorders that may precede loss of visual acuity and observable changes in vascular morphology [1]. Changes in retinal oxygen consumption could affect the blood oxygen saturation (sO_2), which is the ratio of oxygenated hemoglobin to the total hemoglobin concentration in arteries and veins. If quantified accurately, sO_2 could be used as a biomarker to monitor retinal metabolism and provide a valuable early indicator of ocular disease.

Non-invasive retinal sO_2 assessment relies on the absorption contrast of oxy- and deoxy-hemoglobin. Using fundus photography [2] and scanning laser ophthalmoscopy [3], it can be calculated from the optical density ratio between two wavelengths. However, accurate quantification has been restricted by the two-dimensional nature of these technologies, which can neither distinguish blood vessels at different depths, nor separate hemoglobin absorption from other retinal pigments, such as melanin. Zhang *et al* developed photoacoustic microscopy (PAM), which uses multi-wavelength measurements to provide depth-resolved sO_2 [4, 5]. This method, while more robust, requires an ultrasound detector in contact with the eyelid to collect the retinal thermoelastic expansion after laser excitation.

Optical coherence tomography (OCT) [6] is an imaging technology of great utility in ophthalmology due to its ability to visualize and quantify pathological changes in the retina [7]. Standard OCT has been explored for oximetry by using the isosbestic points of oxygenated hemoglobin and deoxygenated hemoglobin around 800 nm. However, this approach has limited accuracy, since the extinction due to light absorption in the near infrared is overwhelmed by scattering [8]. Recently, visible light OCT (vis-OCT) was designed to quantify sO_2 in the retina for the much higher absorption coefficients of hemoglobin in the visible range [9], achieving a superior performance over standard OCT [10, 11]. As vessels can be isolated in the depth profile (A-line) with a high axial and transverse resolution, the absorption spectrum of highest signal-to-noise ratio from the posterior vessel borders can be used for optimal sO_2 measurement since 1) the accumulated absorption is greatest in the posterior vessel boundary and 2) the reflectance signal is usually strong, due to the large refractive index discontinuity [12]. However, to date this technique has been hampered by the need to locate the posterior boundary manually, which is laborious and introduces a large inter-grader variation.

We have recently reported a fiber-based [13] compact vis-OCT system [14] for high-resolution structural and angiographic imaging. Here, we use this to implement a non-invasive spectroscopic retinal oximetry algorithm for assessing retinal blood sO_2 in rats [9,

15]. In contrast to previous studies, the posterior vessel boundaries are automatically detected on structural OCT for a more reliable and objective calculation of sO_2 .

2. Theory

2.1 Hemoglobin contrast

Retinal oximetry utilizes the absorption contrast of oxygenated hemoglobin (HbO_2) and deoxygenated hemoglobin (Hb) to measure sO_2 [16]. Compared to a standard OCT operating in the near infrared, vis-OCT provides several advantages for blood oxygen saturation measurement [Fig. 1]. First, the extinction coefficients of HbO_2 and Hb are two-orders of magnitude stronger in the visible range than in the infrared. Second, confounding absorption from water molecules is nearly absent in the visible range [17]. Third, the absorption characteristics of HbO_2 and Hb have much better contrast for spectroscopic analysis in the visible range, showing remarkable peaks that can be distinguished in the logarithm extinction coefficient curve (HbO_2 : 540 nm and 575 nm, Hb : 555 nm).

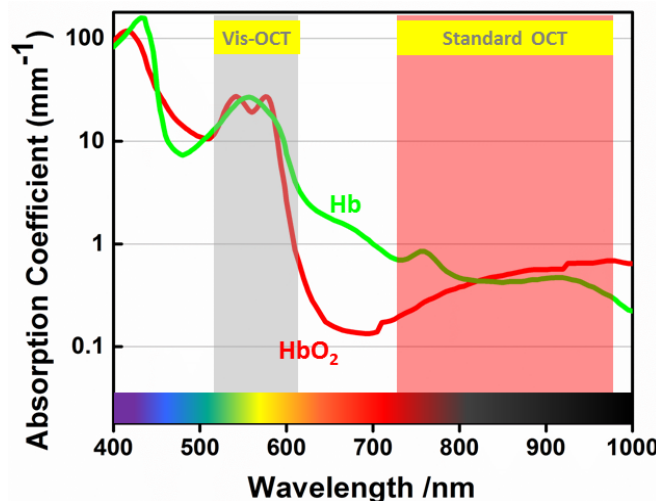


Fig. 1. Logarithmic absorption extinction coefficients of oxygenated hemoglobin (HbO_2) and deoxygenated hemoglobin (Hb) in the wavelength range from 400 nm to 1000 nm [16]. The much higher extinction coefficients in the visible range (vis-OCT) compared to the infrared range (standard OCT) provides a better contrast to quantify oxygen saturation (sO_2).

Assuming C_{HbO_2} and C_{Hb} , the concentrations of HbO_2 and Hb , are uniform in one vessel, the wavelength-dependent A-line reflectance intensity $I(z, \lambda)$ could be expressed as Eq. (1), where z_0 is the depth of the vascular anterior boundary, $I_0(\lambda)$ is the incident spectrum, R_0 is the wavelength independent reference arm reflectance and $r(\lambda)$ is the reflectance in the vessel, which is wavelength-dependent and can be modeled as a power law $r(\lambda) = A\lambda^{-\alpha}$ under the first-order Born approximation [18]. The effective extinction coefficients of HbO_2 and Hb are annotated by $\epsilon_{HbO_2}(\lambda)$ and $\epsilon_{Hb}(\lambda)$ [16].

$$I(z, \lambda) = I_0(\lambda)R_0r(\lambda)e^{-2(z-z_0)[C_{HbO_2}\epsilon_{HbO_2}(\lambda)+C_{Hb}\epsilon_{Hb}(\lambda)]} \quad (1)$$

Taking the natural logarithm of the normalized spectrum, a linear expression for the optical depth OD can be derived using [Eq. (2)]. By this expression, the oxygen saturation sO_2 in any vessel can be calculated as $C_{HbO_2} / (C_{HbO_2} + C_{Hb})$, which is the ratio of oxygenated hemoglobin to the total hemoglobin concentration.

$$OD(z, \lambda) = \ln\left(\frac{I(z, \lambda)}{I_0(\lambda)}\right) = -2(z-z_0)[C_{HbO_2}\epsilon_{HbO_2}(\lambda)+C_{Hb}\epsilon_{Hb}(\lambda)]-\alpha\ln(\lambda)+\ln(AR_0) \quad (2)$$

Wavelength-dependent $OD(z, \lambda)$ can be extracted by short time Fourier transform spectroscopic analysis, which is similar to the split-spectrum analysis in our previous publications [19, 20] but typically has a larger number of spectral bands. Here, Gaussian window groups with a full-width at half-maximum of approximately 9 nm and an interval distance around 3 nm were applied to the interference spectrum, yielding a total of 21 split spectra and reducing the axial resolution to 12 μm (10 times the 1.2 μm axial resolution for the structural image).

2.2 Spectroscopic fitting

To perform the spectroscopic fitting, the linear equation can be rewritten as a matrix product along the wavelength dimension (Eq. (3) [9, 15]. Assuming the number of split spectra is n ($n = 21$ in this study), the size of the matrix \mathbf{OD} on the left side of Eq. (3) is $n \times 1$. The first matrix in the right-hand side is an $n \times 4$ coefficient matrix \mathbf{M}_c , containing the extinction coefficients that can be found in the literature [16]. Then the 4×1 matrix \mathbf{F} can be fitted by a nonnegative least-square fitting model. Since the values of the first and second terms in matrix \mathbf{F} are proportional to concentrations of HbO_2 and Hb , the sO_2 can be calculated as $sO_2 = \mathbf{F}(1)/(\mathbf{F}(1) + \mathbf{F}(2))$.

$$\begin{bmatrix} OD(z, \lambda_1) \\ OD(z, \lambda_2) \\ \dots \\ OD(z, \lambda_n) \end{bmatrix} = \begin{bmatrix} \varepsilon_{\text{HbO}_2}(\lambda_1) & \varepsilon_{\text{Hb}}(\lambda_1) & \ln(\lambda_1) & 1 \\ \varepsilon_{\text{HbO}_2}(\lambda_2) & \varepsilon_{\text{Hb}}(\lambda_2) & \ln(\lambda_2) & 1 \\ \dots & \dots & \dots & \dots \\ \varepsilon_{\text{HbO}_2}(\lambda_n) & \varepsilon_{\text{Hb}}(\lambda_n) & \ln(\lambda_n) & 1 \end{bmatrix} \begin{bmatrix} -2(z - z_0)C_{\text{HbO}_2} \\ -2(z - z_0)C_{\text{Hb}} \\ -\alpha \\ \ln(AR_0) \end{bmatrix} \quad (3)$$

The effective extinction coefficients $\varepsilon_{\text{HbO}_2}(\lambda)$ and $\varepsilon_{\text{Hb}}(\lambda)$ contain both absorption and scattering contributions. The blood optical scattering originates from the refractive index mismatch between red blood cells and plasma. Absorption of hemoglobin actually affects the scattering by multiple scattering processes and causes an oxygen saturation-dependent scattering spectrum. By using this coefficient rather than the absorption of hemoglobin alone, the equation better represents the interaction of light with blood as it travels through the vessel [16].

3. Method

3.1 Blood flow phantom

Human whole blood was anticoagulated and separated into two portions. One portion was ventilated with pure oxygen for 40 mins and shaken simultaneously to fully oxygenate the hemoglobin. The other portion was ventilated with pure nitrogen gas to get a strongly deoxygenated blood sample. After that, blood samples with different sO_2 levels were produced by mixing the fully oxygenated and strongly deoxygenated whole blood at different ratios. In total, 9 samples were obtained and sealed with mineral oil where the volume portion of fully oxygenated whole blood was 0%, 12.5%, 25%, 37.5%, 50%, 62.5%, 75%, 87.5% and 100% respectively. The pH for the blood samples was measured to change from 7.383 to 7.423, increasing with the volume proportion of fully oxygenated hemoglobin.

The sO_2 in each sample was measured as SpO_2 by a commercial blood gas analyzer (i-STAT, Abaxis). A syringe pump (70-2208, Harvard Apparatus) was used to control blood flow through a glass tube ($d = 0.28$ mm). An objective lens (LSM03-VIS, Thorlabs) focused the light beam onto the tube. One hundred repeated B-scans were acquired at the same y-location to obtain sO_2 results.

3.2 Animal preparation

Brown Norway rats (17 weeks old) were initially anesthetized with 5% isoflurane in a sealed box for 10 mins, followed by 2.5% isoflurane during the imaging session. After induction of

anesthesia, the animal was immobilized in a custom-made imaging stage with multidimensional adjustment [14]. The pupil was dilated with a 0.5% tropicamide ophthalmic solution before imaging. To keep the cornea moisturized, sterile irrigating salt solution (Alcon Laboratories Inc.) was applied to the eye every other minute. The animal's body temperature was maintained at 38.5 °C with a water warming blanket.

To regulate the oxygen concentration in the inhalation gas, rats were ventilated via a custom nose cone with a mixture of oxygen and room air. The ratio of the two gases was controlled by a high flow Air-Oxygen Blender (PM5200, Precision Medical) and the oxygen concentration was recorded by an oxygen monitor (PM5900, Precision Medical). The exhaust gas was removed by a vacuum pump to avoid carbon dioxide accumulation and exhaled isoflurane was collected by an anesthesia gas filter (OMNICON F/air, Bickford) before releasing to the open air. The systemic arterial oxy-hemoglobin saturation (SaO_2), as well as heart rate and breathing rate were recorded by a pulse oximeter (MouseOx Plus, STARR) attached to the left rear paw of the animal. For each inhaled gas concentration, the animal was allowed to rest for at least 3 minutes, and the image was taken only after the SaO_2 reading stabilized.

All the experimental procedures were approved by the Institutional Review Board/Ethics Committee and the Institutional Animal Care and Use Committee (IACUC) of the Oregon Health & Science University (OHSU).

3.3 Data acquisition

Measurements were obtained using a custom-made, fiber-based vis-OCT system for rodent retinal imaging [14]. Briefly, the working spectrum range is within 510 nm to 610 nm to cover the high absorption contrast region of hemoglobin. To achieve a better collecting efficiency for the reflected light from the retina, an unbalanced 90:10 wideband fiber optical coupler split the light beam and guided 10% of the power into the sample arm. A telescope tube ($f_1 = 75 \text{ mm}$, $f_2 = 15 \text{ mm}$) delivered the light beam into the eye. Proper focusing on the retina was evaluated by inspection of the *en face* OCT reflectance projection view.

Volumetric raster scans were collected over a $2.2 \times 2.2 \text{ mm}^2$ area at a 50-kHz A-line rate. Three B-scans, each consisting of 512 A-lines, were captured at each of 512 locations in 17 seconds. The oxygen concentration in the inhalation gas was adjusted to 100%, 50%, 21%, back to 50% and then 100%. After scanning, the eyes were further examined by fundus imaging (Micron IV, Phoenix Research Labs). Circular Doppler scans ($d = 0.9 \text{ mm}$) consisting of 4096 A-lines were also acquired around the disc and the Doppler phase shift was calculated between adjacent A-lines to determine flow signals along the axial direction. Six rat eyes were imaged using the above oxygen regulation protocol, which was repeated 4 weeks later to assess reproducibility. Parallel computation on the GPU (GeForce, Quadro K420) using CUDA was incorporated in the control software written in C to enable the high speed acquisition and real time view of both the B-scan and *en face* images. After data acquisition, retinal oximetry measurements were performed using a code written in MATLAB.

3.4 Detection of the vascular posterior boundary

When visible light illuminates vessels and interacts with hemoglobin in the red blood cells, the absorption accumulates axially, in the direction of light propagation. Since the maximum absorption is located at the posterior boundaries of vessels and the reflectance at the vessel wall is larger than the lumen reflectance, the optical depth is calculated at this position. The superiority of choosing the vessel's posterior voxels in sO_2 measurement has been proven experimentally [15], where the highest R-square values were found at the posterior boundaries.

Assuming vessels are cylinders [Fig. 2(A)], the vessel shape on cross-sectional OCT will always be elliptical, with the major axis length modulated by the angle θ between blood flow

direction and the light scanning plane (B-scan). Therefore, the anterior and posterior boundaries of the vessel on cross-sectional structural OCT (B-scan) are symmetric. To obtain the coordinates of the vascular posterior boundaries, the centerlines of the vessels (x_c, y_c) were first automatically detected on the *en face* OCT reflectance projection image (blue line in Fig. 2B). The anterior borders of retinal major vessels can be segmented by directionally graph-searching the inner limiting membrane [21]. Then, the vascular posterior boundary can be symmetrically localized by using the known vessel depth diameter H , determined as the distance between the corresponding anterior boundary voxel at x_c and the last suprathreshold voxel (at 2.5 times the mean intensity of the cropped A-line). Technically, the anterior boundary was rotated 180° (dashed red curve) at their x_c positions and then moved H voxels down (solid red curve) to acquire the vascular posterior boundary [Fig. 2(C)].

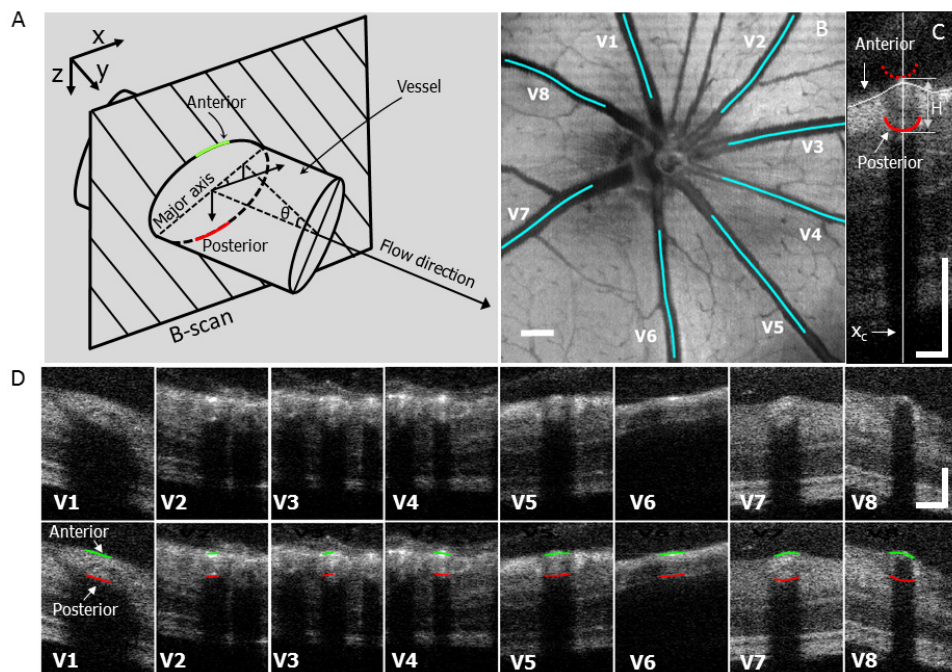


Fig. 2. Posterior vessel boundary detection in the rat retina. (A) Vascular cross-section ellipse in the B-scan. θ : angle between the B-scan plane and normal direction of blood flow. (B) Vascular centerline extraction. Scale bar = 200 μm . (C) Vascular posterior boundary detection in B-scan. Scale bar = 100 μm . (D) The detected posterior boundaries (red) for eight vessels, compared to their anterior borders (green). Scale bar = 100 μm .

By visual inspection, the detection accuracy of posterior boundaries is satisfying [Fig. 2(D)], even in vessels that are severely affected by “fringe washout” (e.g. V8 in Fig. 2D) with signal loss inside the vessel cavity. Note that, since the spectroscopic fitting results are related to absorption optical length, only voxels near x_c with similar absorption optical lengths, were averaged together [red mark in Fig. 3]. For each vessel, nine transverse positions around x_c and five depth voxels near the identified vessel posterior borders were averaged to reduce the spectrum speckle noise. The fitted sO_2 values along the depth of selected voxels [Fig. 3] supports the effectiveness of the identified posterior voxels.

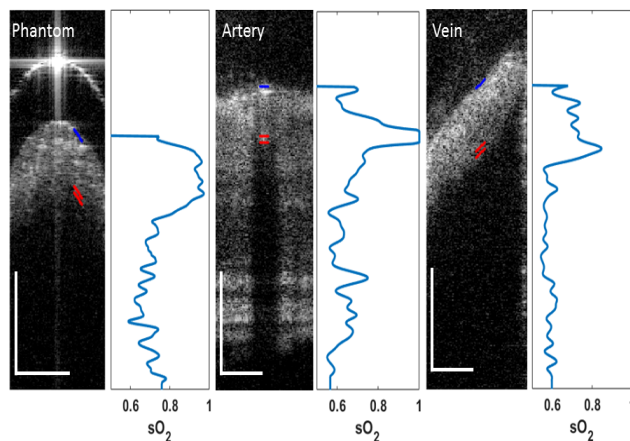


Fig. 3. Enlarged B-Scans marked with the identified voxels (blue: anterior voxels, red: selected posterior voxels) and the fitted sO_2 along the depth of selected voxels for blood sample at $SpO_2 = 97\%$ (left), an artery at 100% O_2 (center) and a vein at 100% O_2 (right). Scale bar = 100 μm .

4. Results

4.1 In vitro verification

The SpO_2 was measured as 100% for the fully oxygenated blood sample and 60% for the highly deoxygenated blood sample [Fig. 4]. The SpO_2 in other samples increased linearly between 60% and 100% with the volume proportion of fully oxygenated blood sample. sO_2 measured by vis-OCT demonstrated very good agreement with the measured SpO_2 (slope = 1.00, R-square > 0.99).

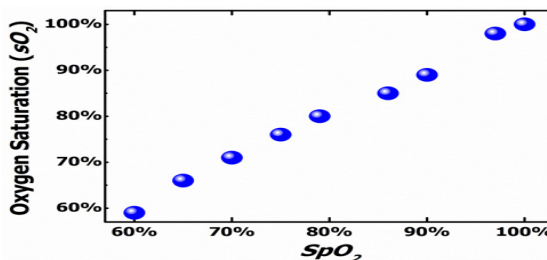


Fig. 4. *In vitro* validation of the algorithm using flow phantom experiments with whole human blood. The fully oxygenated and highly deoxygenated blood samples were mixed at different ratios to vary the sO_2 in blood from 60% to 100%. The sO_2 determined by vis-OCT agreed well with SpO_2 values determined by blood gas analyzer.

4.2 Rat retina arteriovenous identification

Under normoxic conditions [Fig. 5(a)–(c)], arteries (red) had higher sO_2 than veins (green). The arteriovenous identification was supported by their morphologic appearance on fundus images, where arteries tend to have a smaller diameter, stronger reflection and lighter color than veins [Fig. 5(d)–(f)]. This identification of arteries and veins was also corroborated by Doppler OCT, with arterial flow noted to be away from the optic disc, creating a positive Doppler shift (red color in Fig. 5(g)–(i)), and veins flowing toward the disc, with a negative shift (blue color in Fig. 5(g)–(i)).

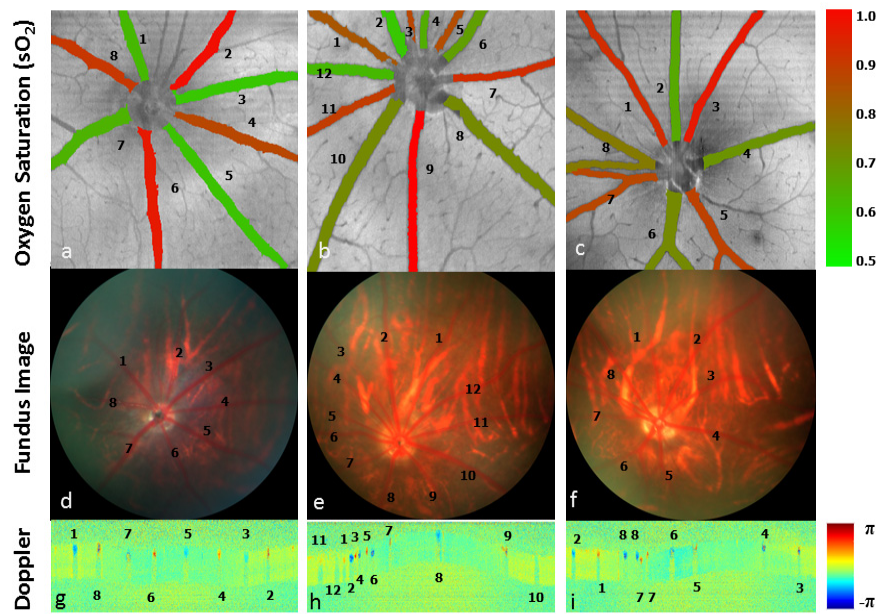


Fig. 5. (a)-(c): Arteries demonstrate higher oxygen saturation (sO_2) than veins by visible light OCT oximetry. Red: artery. Green: vein. The sO_2 of each vessel is overlaid on structural *en face* images. (d)-(f): Fundus images. (g)-(i): Doppler OCT images around the optic disc show opposite flow directions between arteries and veins.

4.3 Oxygen extraction at hyperoxia and normoxia

To demonstrate the capability of the proposed method to evaluate oxygen saturation *in vivo*, we then demonstrated the vascular sO_2 response in vessels at different inhaled O₂ concentrations in one representative eye [Fig. 6]. First, the sO_2 in each major vessel was successfully obtained. The variation trends of sO_2 responding to the inhaled O₂ concentrations corresponded to the variation of SaO₂ readings (see details in Sect. 4.4), but the response amplitudes were very distinct between arteries and veins. Veins appeared to react more to the reduction of oxygen concentration and demonstrated a larger drop in sO_2 at normoxia. Accordingly, the oxygen extraction (the difference between averaged arterial sO_2 and venous sO_2) increased from 12% at hyperoxia (100% inhaled O₂) to 29% at normoxia (21% inhaled O₂).

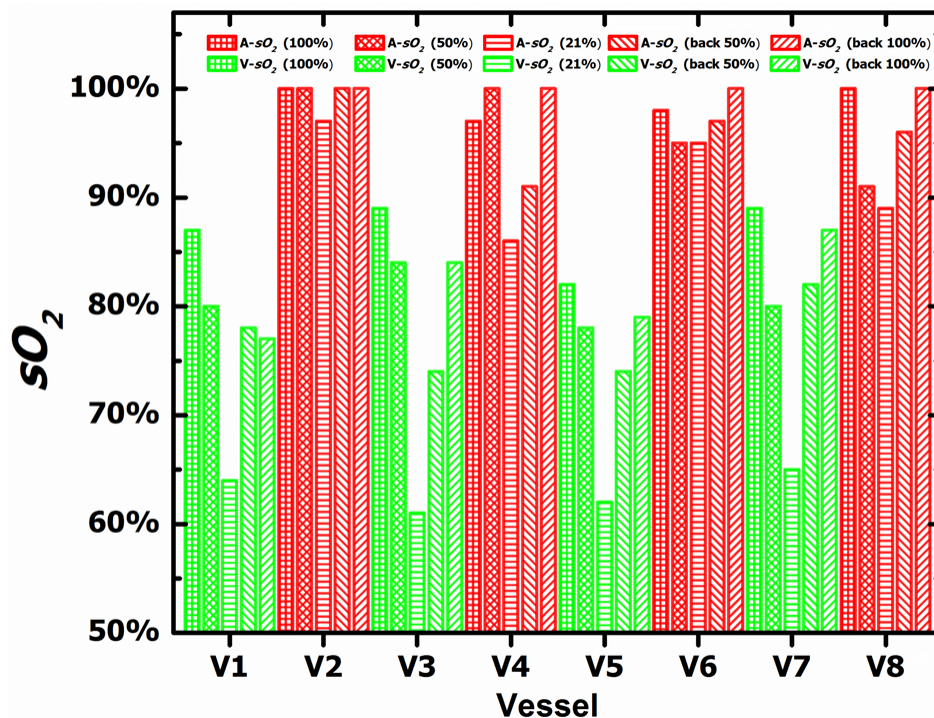


Fig. 6. Representative sO_2 response of each major vessel (red: arteries, green: veins) in one rat retina to changes in oxygen concentration in the inhalation gas from 100% to 50% and to 21%, and then back to 50% and finally 100%.

To better visualize the response of oxygen extraction to oxygen concentration in a group of rats, the sO_2 values in 58 vessels from 6 eyes were scatter-plotted against the oxygen concentration [Fig. 7]. The arteries and veins were well separated at all conditions, which further supported the ability of this method to distinguish arteries from veins. In addition, arteries demonstrated a larger standard deviation at normoxia compared to other conditions, whereas the standard deviation of veins, noted to be greater than arterial sO_2 at 100% O₂, was nearly constant at all conditions.

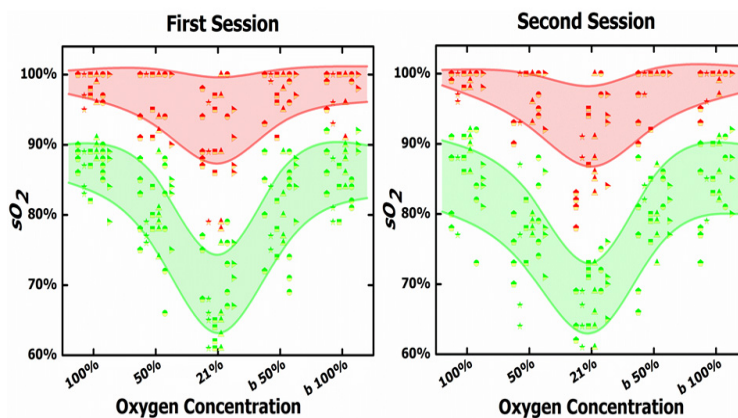


Fig. 7. The oxygen saturation (sO_2) response of arteries (red) and veins (green) to the inhaled oxygen concentration at the first and second sessions, overlaid by the mean \pm standard deviation fitting curve at each oxygen concentration.

The sO_2 values of all animals (Table 1) showed that arterial sO_2 was $99\% \pm 1\%$ and the venous sO_2 was $87\% \pm 2\%$ for the first session during hyperoxia (100% inhaled O₂). During normoxia (21% inhaled O₂), arterial sO_2 dropped to $92\% \pm 4\%$ and venous sO_2 to $69\% \pm 4\%$, suggesting that oxygen extraction (A-V sO_2) increased from 12% to 23% when breathing room air. Oxygen extraction returned to original levels when the inhalation gas was returned to hyperoxia. During the second session, oxygen extraction was 14%, 20%, 22% and then recovered to 18% and 14% during each condition.

Table 1. Response of oxygen extraction [mean \pm population standard deviation (std), A-V sO_2] to changes in oxygen concentration and inter-session reproducibility.

Inhaled Oxygen	First session (mean \pm std)			Second session (mean \pm std)			Inter-session reproducibility (Pooled std)	
	A-sO ₂	V-sO ₂	A-V sO ₂	A-sO ₂	V-sO ₂	A-V sO ₂	A-sO ₂	V-sO ₂
O ₂								
100%	99% \pm 1%	87% \pm 2%	12% \pm 2%	99% \pm 1%	85% \pm 3%	14% \pm 3%	0.6%	2.2%
50%	98% \pm 1%	80% \pm 2%	18% \pm 3%	97% \pm 3%	77% \pm 2%	20% \pm 3%	2.0%	2.7%
21%	92% \pm 4%	69% \pm 4%	23% \pm 4%	90% \pm 6%	68% \pm 4%	22% \pm 3%	2.9%	3.6%
Back 50%	98% \pm 1%	80% \pm 3%	18% \pm 2%	98% \pm 2%	80% \pm 3%	18% \pm 2%	1.2%	2.7%
Back 100%	99% \pm 1%	86% \pm 3%	13% \pm 4%	99% \pm 2%	85% \pm 3%	14% \pm 2%	1.1%	3.0%

4.4 Inter-session reproducibility

The arterial sO_2 and venous sO_2 measured in each rat at every oxygen concentration in the two imaging sessions four weeks apart were compared [Fig. 8] and the reproducibility was calculated as the pooled standard deviation of the averaged sO_2 of arteries and veins in each animal's retina. This analysis demonstrated that arterial sO_2 measured by vis-OCT mirrored systemic arterial oxygen saturation (SaO₂) determined by pulse oximetry (correlation: 0.92, p-value<0.001) and confirmed that arteries could be distinguished from veins by vis-OCT oximetry, with a distinctly higher sO_2 in arteries (Fig. 8, red lines) than in veins (Fig. 8, green lines). Finally, the sO_2 response was highly reproducible between the two scanning sessions.

Reproducibility at 21% oxygenation was slightly lower than the other conditions [Table 1, Fig. 8]; which may be due to subject variability. Furthermore, arteries were found to have higher reproducibility (0.6% - 2.9%) than veins (2.2% - 3.6%), which could be explained by the fact that the sO_2 in veins is more susceptible to changes in tissue metabolism and blood flow at different sessions.

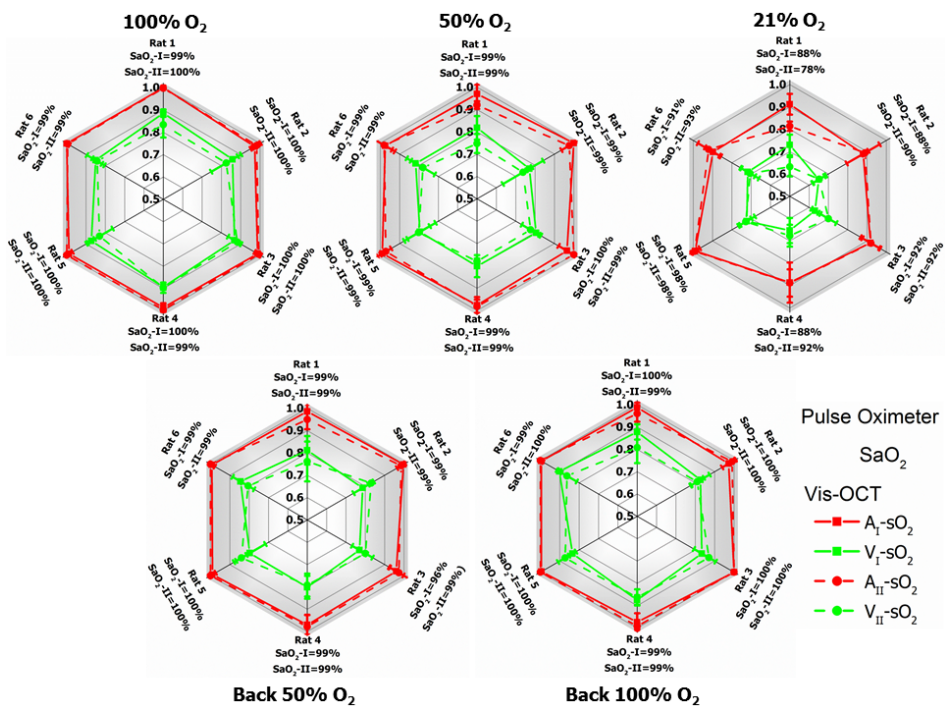


Fig. 8. Comparison of the oxygen saturation between arteries and veins in individual animals at different oxygen concentrations and imaging sessions. Each hexagonal chart represents a certain inhaled oxygen concentration (100%, 50%, 21%, back to 50% and then back to 100%). Each vertex of the hexagons represents the measurements for a given animal (Rat 1-6) under the given oxygen concentration. For each rat, the systemic arterial oxygen saturation SaO_2 measured by a pulse oximeter is provided for both sessions (I and II). The radius of the hexagon represents the $s\text{O}_2$ values between 50% to 100%. The red color represents arterial $s\text{O}_2$ ($A\text{-sO}_2$) whereas the green color represents venous $s\text{O}_2$ ($V\text{-sO}_2$). Typically, $A\text{-sO}_2$ is larger than $V\text{-sO}_2$. Solid lines connect measurements made in the first session (I) and dashed lines connect measurements made in the second session (II). Proximity between the same measurement in two sessions indicates good repeatability.

5. Discussion and conclusion

Using vis-OCT to noninvasively assess oximetry in the retina may have important scientific and clinical implications. Although initial studies demonstrated that $s\text{O}_2$ will vary at different oxygen concentrations [22], this work incorporates several critical improvements. Our fiber-based vis-OCT system provides more efficient power distribution by using an unbalanced fiber coupler, previously reported in Refs [13, 14]. In addition, we have developed an automated algorithm to measure oxygen saturation in rodent retinal blood vessels by automatically segmenting vascular posterior boundaries, which provides an objective quantitative analysis, as opposed to prior methods that selected the interest voxels manually. To validate the performance of our oximetry algorithm, we conducted *in vivo* oxygen challenge experiments in two sessions, four-weeks apart and demonstrated the inter-session reproducibility.

Oximetry based on vis-OCT allows measurement with high spatial resolution down to single retinal vessels, which cannot be achieved by commercially available oximeters that measure systemic arterial oxygen saturation. This differentiation of oxygen saturation between arteries and veins allows us to calculate oxygen extraction, which provides insights into oxygen delivery and tissue consumption. Additionally, this non-invasive measurement allows longitudinal monitoring with high temporal resolution (several seconds). Integrated

with the total blood flow measurements using Doppler OCT, oxygen metabolism in the retina can be examined and monitored with this technique.

Using this system, we noted a clear separation between retinal arterial and venous sO_2 , with the former varying little from 100% to 50% O₂, and then decreasing to 92% and 90% at room air on two separate measurement sessions. By contrast, venous sO_2 , always less than arterial sO_2 , showed a significant change with each level of inspired oxygen, with more pronounced reductions as compared to arterial sO_2 at progressively lower levels of O₂. This result, indicating increased oxygen extraction, is consistent with a previous report that lower levels of inhaled oxygen concentration produced greater reductions in venous than arterial sO_2 , and an increased retinal oxygen metabolic rate, potentially in compensation for reduced oxygen supply in the choroid, which has less efficient autoregulation [22].

We found that, in arteries, sO_2 was less variable at 100% oxygen than at room air, which likely results from the high oxygen affinity of hemoglobin under conditions of high oxygen saturation, and its release at normoxia. Interestingly, at 100% O₂, venous sO_2 variability was greater than that of arteries. This coincides with the fact that venous blood is collected from tissue capillaries while the arterial blood comes directly from central retina artery. Thus the veins would be more likely affected by changes in retinal tissue metabolism and other factors, such as capillary blood flow, between individuals and at different time points, which would produce more diverse sO_2 values.

In summary, the automated spectroscopic retinal oximetry algorithm shown here with good inter-session reproducibility will greatly improve the assessment of sO_2 in major vessels. As this vis-OCT technology gradually develops to better suit the demands of the clinical setting [13], it will prove useful in early disease evaluation for the management of several blinding ocular diseases.

Funding

National Institutes of Health (R01 EY027833, DP3 DK104397, R01 EY024544, R01 EY023285, R01 EY010145, P30 EY010572); unrestricted departmental funding grant and William & Mary Greve Special Scholar Award from Research to Prevent Blindness (New York, NY).

Disclosures

David Huang: Optovue Inc (F, I, P, R). Yali Jia: Optovue Inc (F, P). Miao Zhang: Optovue Inc (E). These potential conflicts of interest have been reviewed and managed by OHSU. Other authors declare that there are no conflicts of interest related to this article.